Elsevier required licence: © <2021>. This manuscript version is made available under the CC-BY-NC-ND 4.0 license http://creativecommons.org/licenses/by-nc-nd/4.0/
The definitive publisher version is available online at
[https://www.sciencedirect.com/science/article/pii/S0045653521004896?via%3Dihub]

Synthesis and NO_x removal performance of anatase S-TiO_2/g-CN heterojunction formed from dye wastewater sludge

Sayed Mukit Hossain [a], Heeju Park [b], Hui-Ju Kang [c], Jong Seok Mun [b], Leonard Tijing [a], Inkyu Rhee [d], Jong-Ho Kim [b,***], Young-Si Jun [c,**,] and Ho Kyong Shon [a,*]

[a] Faculty of Engineering and IT, University of Technology, Sydney, P.O. Box 123, Broadway, NSW 2007, Australia; sayed.m.hossain@student.uts.edu.au (S.M.H.); leonard.tijing@uts.edu.au (L.T.); Hokyong.Shon-1@uts.edu.au (H.K.S.)

[b] School of Chemical Engineering, Chonnam National University, 77 Yongbong-ro, Buk-gu, Gwangju 61186, Republic of Korea; point1014@hanmail.net (H.P.); answhdtjr8726@gmail.com (J.S.M.); jonghkim@chonnam.ac.kr (J.-H.K)

[c] Department of Advanced Chemicals & Engineering, Chonnam National University, 77 Yongbong-ro, Buk-gu, Gwangju 61186, Republic of Korea; gmlwn120@gmail.com (H.-J.K.); ysjun@jnu.ac.kr (Y.-S.J)

[d] Department of Civil Engineering, Chonnam National University, 77 Yongbong-ro, Buk-gu, Gwangju 61186, Republic of Korea; rheei@chonnam.ac.kr (I.R.)

* Correspondence: Hokyong.Shon-1@uts.edu.au (H.K.S.); ysjun@jnu.ac.kr (Y.-S.J); Tel.: +61 447 332 707 (H.K.S.)

Abstract

In this study, sludges generated from Ti-based flocculation of dye wastewater were used to retrieve photoactive titania (S-TiO_2). It was heterojunctioned with graphitic carbon nitride (g-CN) to augment photoactivity under UV/visible light irradiance. Later the as-prepared samples were utilized to remove nitrogen oxides (NO_x) in the atmospheric condition through photocatalysis. Heterojunction between S-TiO_2 and g-CN was prepared through facile calcination (@550 °C) of S-TiO_2 and melamine mix. Advanced sample characterization was carried out and documented extensively. Successful heterojunction was confirmed from the assessment of morphological and optical attributes of the samples. Finally, the prepared samples' level of photoactivity was assessed through photooxidation of NO_x under both UV and visible light irradiance. Enhanced photoactivity was observed in the prepared

samples irrespective of the light types. After one h of UV/visible light-based photooxidation, the best sample STC4 was found to remove 15.18% and 9.16% of atmospheric NO, respectively. In STC4, the mixing ratio of S-TiO_2, to melamine was maintained as 1:3. Moreover, the optical bandgap of STC4 was found as 2.65 eV, where for S-TiO_2, it was 2.83 eV. Hence, the restrained rate of photogenerated charge recombination and tailored energy bandgap of the as-prepared samples were the primary factors for enhancing photoactivity.

Keywords

Resource recovery, TiO_2/g-CN, NO_x photooxidation, Nitrate selectivity, Heterogenous photocatalysis

1 Introduction

In conventional wastewater treatment plants, coagulation and flocculation have been employed for generations for the removal of particulate matters either in suspension or colloidal form. In general, settling basin and mechanical filtration can easily separate the pollutants in suspension but found ineffective in removing colloidal particles (Zhao and Li, 2019). Meanwhile, coagulation and flocculation can readily remove various water-induced contaminants of the colloidal genre, e.g., materials causing turbidity, metal oxides, persistent toxic compounds, organic materials, stable emulsions, etc. (Xia et al., 2018; Zhang et al., 2018b; Hussain et al., 2019). Traditionally, various types of Al and Fe salts are used as coagulants; however, they are induced with the significant drawbacks of unwanted sludge generation and effects of trace metals (Al/Fe) in subsequent effluent (Xu et al., 2018b). Recently, Ti-based salts ($TiCl_4$, $TiSO_4$, and PTC) are found to perform on par with the Al and Fe based coagulants (Wang et al., 2018a; Wang et al., 2018c; Chi et al., 2019). Ti (IV) coagulation has been effectively applied to treat water and wastewater enriched with various types of pollutants, such as inorganic colloids (Wang et al., 2018c), natural organic matter with varying molecular weight (Wan et al., 2019), algae (Xu et al., 2018b; Chi et al., 2019), trace nanoparticles (Aziz et al., 2018), phosphorous (Jeon and Ahn, 2018), arsenic (Sun et al., 2013) and many more. Additionally, Shon et al. (2009b) affirmed equivalent pollutant removal comparing conventional coagulants ($FeCl_3$ & $Al_2(SO_4)_3$) and steady titania recovery from the flocculated sludge (Shon et al., 2007). Photo-catalytically active

anatase TiO_2 were prepared through incineration of $TiCl_4$ flocculated sludge at a temperature of 600 ℃ to 800 ℃. Shortly after, Lee et al. (2008), studied the aquatic toxicity of residual Ti after $TiCl_4$ coagulation. They observed negligible toxicity at a chemical dose of 150 mg/L. Furthermore, the ready titania from flocculated sludge showed low toxicity compared to commercially available TiO_2 (P-25). Hence Ti-based coagulation possesses the potential to mitigate the human health and high chroma index issues of residual Al and Fe after treatment (Lee et al., 2008; Shon et al., 2008; Okour et al., 2009b). To date, titania nanoparticles (NPs) and nanofibers (NFs) have been developed by utilizing the coagulated sludge of drinking water, seawater, biologically treated sewage effluent, wastewater from the printing press, dye wastewater and algae bloomed surface water (El Saliby et al., 2009; Okour et al., 2009a; El Saliby et al., 2010; Kim et al., 2010). The provision of resource recovery as titania (TiO_2) and negligible aquatic toxicity of residual Ti established the background of the current study.

Initially, Fujishima and Honda (1972) announced the revolutionary study on TiO_2 electrode sensitization for H_2O electrolysis. Since then, many research groups have examined the possibility of using TiO_2 as photocatalysts for the hydrolysis of H_2O, towards numerous practical implications (Haider et al., 2019; Wang et al., 2019). Moreover, TiO_2 is cost-effective, non-toxic as a photocatalytic substance, and has reasonably good reactivity and stability in both aqueous and atmospheric environments (Diebold, 2003). TiO_2 has mostly been developed for the application of highly dispersed standalone photocatalysts, dye-sensitized solar cells, and the UV/visible light irradiated degradation of organic and inorganic pollutants through photocatalysis (Asahi et al., 2014; Nasirian et al., 2017). However, the main shortcoming of TiO_2 that has hindered its practical application is its wide energy bandgap of ~3.2 eV (Nasirian et al., 2017). Hence, standalone utilization of TiO_2 for photocatalysis can only be facilitated by light irradiation in the UV region. Moreover, due to having large energy bandgap, the rate of recombination of the developed photoinduced electron/hole (e^-/h^+) pair is elevated, which substantially suppresses the photoactivity of TiO_2 (Asahi et al., 2014). Hence, to overcome the limitations associated with a large energy bandgap, a number of strategies were utilized to augment the photocatalytic efficiencies of TiO_2. To date, the most common strategies that have been employed includes self-structural adjustment, metal/noble metal/non-metal doping, sensitization, and

heterojunction with other suitable semiconductors (Asahi et al., 2014; Nasirian et al., 2017). Among the techniques mentioned above, the heterojunction of semiconductors has stirred outstanding interest in recent years. In the last decades, an N modified TiO_2 was synthesized through pyrolysis of the precursor mix of TiO_2 and urea/melamine at 400 °C, which showed notable photoactivity within the visible light spectrum (Kobayakawa et al., 2005). The aforementioned visible light activation was attributed to the highly condensed melamine products such as melam, melem, and melon, which are the predecessors of graphitic carbon nitride (g-CN) (Zhang et al., 2019a). These research results recommended that the products created from further condensation of melamine can potentially sensitize titania for visible light activation, which may have created an inspirational route of TiO_2/g-CN heterojunction formation. Hence, an extensive research study has been conducted on visible light-sensitive g-CN, focusing on their composition, and structural arrangement to manage the necessary transformation of light energy into usable chemical energy (Ong, 2017; Kumar et al., 2018; Tan et al., 2018; Xiao et al., 2018).

The backbone of g-CN, a nonmetal-based semiconductor, is constructed as a conjugated polymeric system and contains the earth abundant C and N atoms (Xu et al., 2018a). The polymeric layers are being constructed with s-triazine ($C_3H_3N_3$) or heptazine ($C_6H_3N_7$) units interlinked by tertiary amine groups, and the layer atoms are considered in the arrangement of honeycomb. (Kumar et al., 2018). The $C_3H_3N_3$ or $C_6H_3N_7$ based 2D layers remain interconnected through weak van der Waals forces. Hence, due to the presence of aromatic heterocycles, including prevailing van der Waals forces within the polymeric sheets, g-CN is thermally durable up to 600 °C in atmospheric conditions (Zhang et al., 2019a). Also, g-CN showed superior chemical stabilities in solvents like water, alcohols, ethers, and several weak acids. Moreover, the optical bandgap of g-CN is narrower (~2.7 eV), and with respect to normal hydrogen electrode at pH= 7, the conduction band (CB) and valence band (VB) location could be estimated as -1.31 and +1.40 eV, respectively (Zhou et al., 2019). Hence, as a photocatalyst, the extraordinary advantages of g-CN include favorable electro-optical properties and superior visible light sensitivity due to narrow energy bandgap. For the preparation of photocatalytic heterojunction, molecular level chemical modification can easily be applied to facilitate favorable surface properties of g-CN. Moreover, several studies inferred that g-CN showed outstanding compatibility as a host

nanomaterial while composited with diverse inorganic NPs (Zhou et al., 2019; Huang et al., 2020; Yu et al., 2020). However, the prompt recombination of the photogenerated e^-/h^+ pairs and the inferior active surface area is still two vital disadvantages limiting the photoactivity of g-CN. Therefore, developing novel answers to surmount these barriers are of significant importance.

Over the past decades, a substantial increase in atmospheric nitrogen oxides (NO_x; NO + NO_2) has been observed, and photooxidation of NO_x is one of the most prominent solutions for this problem (Ma et al., 2016; Papailias et al., 2017). Many research groups nowadays have focused on this topic and developed a number of efficient photocatalysts to oxidize NO_x into a more neutral product. The suitable positioning of the CB and VB edge of anatase TiO_2 and g-CN, along with the 2D sheet-like structure of g-CN, favors successful heterojunction. It has been reported that g-CN could form a thin layer on TiO_2 NPs, while heterojunction is formed (Jiang et al., 2018). Additionally, type II heterojunction has been reported for anatase TiO_2/g-CN composites due to the placement of their CB and VB edges (Ma et al., 2016). Therefore, photogenerated e^- and h^+ can migrate between the band edges of TiO_2 and g-CN, facilitating the hindered rate of recombination. Giannakopoulou et al. (2017) demonstrated an easy solvent-free mechanical mixing followed by calcination technique to tailor the energy bandgap of TiO_2/g-CN, to facilitate NO oxidation. They oxidized an initial concentration of 1 ppm NO under both visible (7000 lux) and UV (10 Wm^{-2}) light irradiation. After 40 min of irradiance, they attained a maximum of 38% and 42% of removal for visible and UV light, respectively. Papailias et al. (2017) similarly removed NO_x using TiO_2/g-CN with a removal rate of 18% and 22.5% after 30 min by using visible and UV irradiation, respectively. This was attained by modifying the surface morphology of the as-prepared photocatalysts with the assistance of $CaCO_3$. Recently, Huang et al. (2019) used a simple ultrasonic exfoliation technique and synthesized Ti^{3+} TiO_2/p-CN composite for the purpose of NO_x oxidation. Using an initial NO concentration of 400 ppb, a removal percentage of 25.8% after 30 min of irradiation was reported.

Despite numerous studies conducted for NO_x removal using TiO_2/g-CN composites, in most cases, commercially available titania was used as the precursor of TiO_2, which increases costs for photocatalyst synthesis. Therefore, in this study, we have synthesized a novel TiO_2/g-CN heterojunction

by using sludge generated titania (S-TiO_2) as the precursor of TiO_2. We have used a template-free approach and utilized the precursor mix of S-TiO_2 and melamine for successful heterojunction. Advanced chemical, morphological and optical characterizations of as-synthesized samples have been conducted. ISO 22197-1 (2007) and ISO 17198-1 (2018) was followed to evaluate the prepared samples' NO_x photooxidation capacity under UV and visible light, respectively. Besides, nitrate selectivity of the ready samples was assessed and based on the advanced characterizations, a possible photooxidation scheme was proposed.

2 Materials and methods

2.1 Preparation of S-TiO_2 from dye wastewater sludge

The wastewater produced by a dye wastewater treatment plant located in Daegu, South Korea, was collected for the purposes of this study. The initial physicochemical properties were as follows: pH, 11.7; chemical oxygen demand (COD), 449 mg/L; total nitrogen (TN), 72 mg/L; total phosphorous, 3.2 mg/L. The wastewater was treated with an optimized dose of $TiCl_4$, which was first rapidly mixed within the sample at a rate of 100 rpm for 1 min before being slowly mixed at a rate of 30 rpm for a further 20 min. The flocculated wastewater was subsequently stored to allow the flocks to settle, after which the settled dye wastewater sludge was extracted dried overnight in a laboratory oven at a temperature of 100℃. A pestle and mortar was used to mill the dried material into a powder form before the anatase S-TiO_2 was synthesized by placing the powder into an alumina crucible and calcining it at 600 ℃ (@10℃/min) for 3 h.

2.2 Preparation of S-TiO_2/g-CN heterojunction

The pure g-CN and conjugated S-TiO_2/g-CN was prepared via a facile one-step synthesis scheme. A box furnace was utilized for annealing the dry mixture of S-TiO_2 and melamine (Sigma-Aldrich, 99%) for the sample preparation. The annealing was performed under atmospheric pressure. Various samples were created by differing the ratio of wt.% of melamine to S-TiO_2, and a calcination temperature of 550 ℃ was applied. The temperature of the box furnace was fixed such that it rose at 10 ℃/min with a calcination duration of 3 h. Table 1 presents an overview of the nomenclature of the prepared samples together with details of the mixing ratios of the precursors.

Table 1. Nomenclatures and salient features of the prepared samples. STC indicates the S-TiO_2/g-CN samples at various melamine concentrations.

ID	Amount(g)		Prepared sample (g)	Mixing ratio	Temperature (°C)	Ramp (°C/min)	Duration (h)
	S-TiO_2	Melamine					
STC1	4	2	4.8	2:1	550	10	3
STC2	4	4	5	1:1	550	10	3
STC3	4	8	7.8	1:2	550	10	3
STC4	4	12	8.1	1:3	550	10	3
STC5	4	16	11	1:4	550	10	3
STC6	4	20	13.2	1:5	550	10	3
g-CN		5	1.1		550	10	3

2.3 Characterization

X-ray diffraction (XRD) analysis was performed to characterize the crystalline phase of the synthesized samples. XRD patterns were generated on an MDI Jade 5.0 X-ray diffractometer (D/MAX Ultima Ⅲ, Rigaku, Japan) operating at 40 kV and 40 mA that was fed with a Cu Kα radiation source. By using the Bragg-Brentano experimental method, the patterns of XRD were documented at a scanning rate of 0.02/sec. Besides, the patterns were generated within the scattered angle (2θ) array of 5° to 90°. The X-ray beam was operated with limiting parameters of 2/3° divergence, 10 mm divergent altitude, 0.3 mm receiving slits, and 2/3° scattering.

A scanning electron microscope (S-4700, Hitachi, Japan) that was operated at 15 kV in a vacuum with a working gap of 7 mm was used to examine the morphology of the powdered S-TiO_2/g-CN. A scanning electron microscope that was supplied with an energy dispersive X-ray detector (55VP SEM) operating at 15 kV was employed to perform the elemental composition analyses. To further investigate

the samples' crystallinity and internal structure, a transmission electron microscope (FE-TEM, JEOL Ltd., JEM-2100F, Japan) was utilized. The TEM samples were prepared by evaporating a droplet of the powders placed on a Cu grid coated with holey carbon support films in ethanol. The as-prepared samples' effective surface area was estimated using the Brunauer-Emmett-Teller (BET) theory. The adsorption-desorption isotherms were generated in Belsorp mini Ⅱ, BEL, Japan. The desorption data was subsequently used in combination with the Barrett-Joyner-Halenda (BJH) framework to investigate the pore volume distributions.

To confirm the presence of anatase titania and g-CN, the IR Prestige-21, Shimadzu, Japan, was utilized to generate the Fourier transform infrared (FT-IR) patterns of the as-prepared samples. The range of wavenumbers was prefixed between 400 cm^{-1} and 4000 cm^{-1}; moreover, the samples were prepared using the KBr pellet preparation method. The X-ray photoelectron spectroscopy (XPS) spectra of the dry samples were generated on a MultiLab2000, VG, UK, to validate the various chemical bonds present in the samples. The photoluminescence (PL) spectra were generated on a dual microplate spectrofluorometer, Horiba, Piscataway, NJ, USA, to evaluate the charge recombination rates of the prepared samples during photoactivity. A sample excitation wavelength of 300 nm was utilized in the fluorometer. A UV-Vis-NIR spectrometer (Lambda 950, Perkin Elmer, KBSI Daegu center, South Korea) that was fitted with a diffuse reflectance (DRA) accessory was used to obtain the UV-VIS spectra, which were documented in a spectral range of between 400 and 800 nm.

The optical bandgaps of the as-prepared samples were determined by using the modified Kubelka-Munk functions illustrated in the following equations,

$$F(R) = \frac{K}{S} \quad (1)$$

$$K = (1 - R)^2 \quad (2)$$

$$S = 2R \quad (3)$$

Here, F(R) is the Kubelka-Munk function, and the K, R, and S are molar absorption coefficient, scattering factor, and reflectance data, respectively. Additionally, for sludge generated titania

(anatase), an indirect energy bandgap was considered, and it was determined through extrapolation of $F(R)h\nu)^{1/2}$ vs. hν. In contrast, the bandgaps of the as-prepared samples were estimated considering direct energy bandgap $(F(R)h\nu)^2$ vs. hν).

2.4 Photocatalytic activity

Following ISO 22197-1 (2007) and ISO 17198-1 (2018) conventions, the as-prepared samples' NO_x removal capacity was investigated under UV and visible light irradiation, respectively. In a continuous flow reactor, the samples were placed and irradiated (pretreatment) at a light intensity of 10 W/m^2 for 5 h. For the pretreatment, two UV-A lamps from Sanyo-Denki, Japan were used. The experimental procedures that were followed are explained in previous work (Rhee et al., 2018).

Briefly, a rectangular sample holder with the surface area of 50 cm^2 was utilized for holding 1 g of uniformly distributed samples. At the inlet of the flow reactor, the ambient parameters were prefixed following the aforementioned ISO protocols. At the reactor's inlet, the moisture content and temperature were maintained as 50% and 25 ℃, respectively. For UV and visible light irradiation, UV-A lamps at a light intensity of 10 W/m^2 ± 0.5 W/m^2 and white fluorescent lamps (with UV cut-off filter) at an intensity of 6000 Lx ± 300 Lx was utilized, respectively. To assess the prepared samples' photoactivity, each time the light irradiation was maintained for 1 h. Besides, a constant airflow of 3 L/min was retained at the inlet to facilitate a continuous flow of 1 ppmv of NO. The subsequent concentrations NO_x, NO, and NO_2 were recorded on a NO_x analyzer (CM2041, Casella). For each sample, the photocatalytic experiment was continued for 100 min, where 20 min of gas adsorption and 20 min of gas desorption were considered at the beginning and end of light irradiation. A simple schematic of the utilized experimental setup is illustrated in Fig. S1. The NO and NO_x removal rate along with the NO_2 generation rate and nitrate (NO_3^-) selectivity were estimated using the following equations,

$$NO_{removal}(\%) = \frac{NO_{in} - NO_{out}}{NO_{in}} \times 100 \quad (4)$$

$$NO_{2,generation}(\%) = \frac{NO_{2,out} - NO_{2,in}}{NO_{in}} \times 100 \quad (5)$$

$$NO_{x,removal}(\%) = \frac{NO_{x,in} - NO_{x,out}}{NO_{in}} \times 100 \quad (6)$$

$$NO_{3^-selectivity}(\%) = \frac{NO_{x,removal}}{NO_{removal}} \times 100 \quad (7)$$

3 Results and discussion

3.1 Photocatalytic activity

The photoactivity of the synthesized samples was assessed through estimating the extent of NO oxidation under UV and visible light irradiance. In addition, the photoactivity of the as-prepared samples were compared with standalone use of S-TiO_2, NP400, and g-CN. Fig. S2 and S3 show the NO, NO_2, and NO_x concentration trends of as-prepared samples, STC1 – STC6, S-TiO_2, NP400, and g-CN, under light (UV/visible) irradiance. Moreover, the detailed results of total NO and NO_x removal along with NO_2 generation during 1 h of light irradiation are tabulated in Table S1 (UV light) and S2 (visible light). For each experiment, 7.58 ± 0.069 µmol NO was inserted in the reactor, and irrespective of the light types (UV/visible), both S-TiO_2 and NP400 showed similar NO removal profile as illuminated in Fig. S2(a) and (h), respectively. For all the samples examined, the NO and NO_x concentrations initiated to decrease instantly at the light irradiance (UV/visible) and reached the minimum concentration of NO and NO_x within 5 min of light irradiation. Negligible response lag was witnessed at the beginning and the end of the light irradiation due to the instrument's default factory setup. The rapid degradation of NO at the starting of the light irradiance could be attributed to the dual effects of adsorption and photooxidation on the photocatalytic sites of the respective samples. Later, due to saturation of the photocatalytic sites with the protoxidized by-products (i.e., NO_2, NO_3^-), the NO removal efficiencies tend to decrease gradually (Park et al., 2014). Fig. S2 and S3 show that the gradual decrease in NO and NO_x removal with irradiation time is dominant in S-TiO_2 and NP400. Interestingly, compared to anatase titania (S-TiO_2 and NP400), the as-prepared samples (STC1-STC6) and g-CN showed stable NO and NO_x removal within 1 h of irradiation (UV/visible), which could be the indication of superior photoactivity.

Fig. 1(a) and (b) reveal the corresponding NO removal, NO_2 generation, and NO_3^- selectivity of the as-synthesized samples along with S-TiO_2, NP400, and g-CN under UV and visible light, respectively. The S-TiO_2 prepared from flocculation of dye wastewater showed very limited

photoactivity under any kind of light irradiation, whether UV or visible light, which is in contrast with some related studies (El Saliby et al., 2012). Under 1 h of UV and visible light irradiation, S-TiO_2 only removed 0.378 µmol and 0.303 µmol of NO, respectively (see Table S1 and S2), which is around 5% of the total NO inserted in the reactor. On the other hand, with the same setup, NP400 showed around 22.89% and 9.36% NO removal under UV and visible light, respectively. As Fig. 1(a) illustrates, the prepared samples under UV irradiation showed significant improvement in NO removal. STC1 showed the maximum NO removal of 25.25%, which is around 5 times higher compared to S-TiO_2. During the synthesis of the sample STC1, the precursor mix contained around 33.33% (Table 1) of melamine, and in the following samples, the melamine contents were increased as 50%, 66.67%, 75%, 80%, and 83.33%. With increased melamine content in the precursor mix, at 50% melamine content, the NO and NO_x removal get reduced to 17.03% and 6.92%, respectively. Later, at 75% melamine content, the sample showed enhanced NO_x removal of 7.82%, and a further increase in melamine content within the precursor showed a consecutive reduction in NO and NO_x removal. One dominant trait that has been observed is, with increased melamine proportion in the precursor mix, the NO_3^- selectivity of the samples showed an increasing trend and begun to decline while the melamine proportion exceeded 75% of the initial mix.

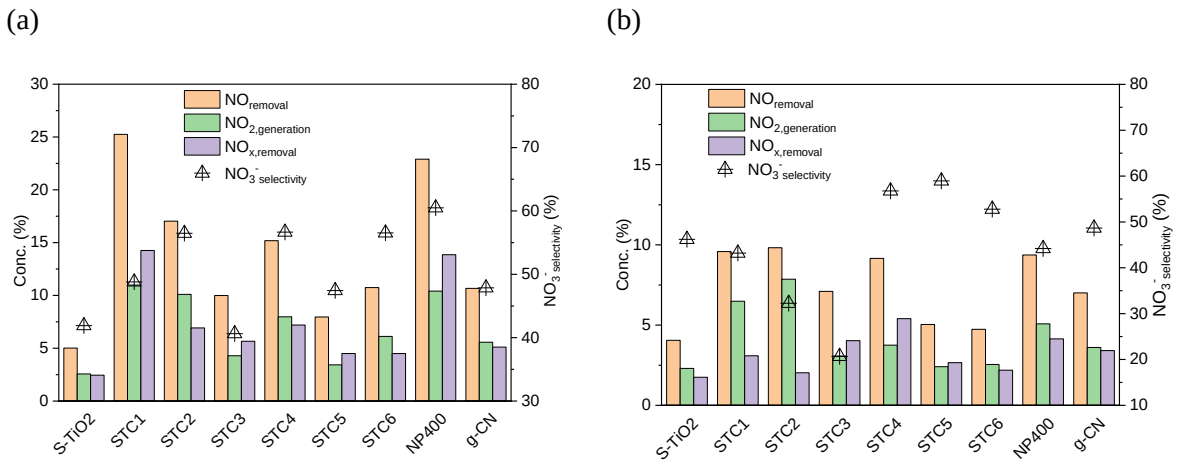

Fig. 1. NO_x removal and NO_3^-selectivity of the as-prepared samples under 1 h of (a) UV light, and (b) visible light irradiation.

Fig. 1(b) shows that STC4 achieved the maximum NO_x removal of 5.4% under visible light due to superior NO_3^- selectivity of 56.76%. As illustrated in Table S2, in total, 7.63 ± 0.067 µmol NO_x was inserted in the reactor under visible light irradiation of 1 h for each sample. At the end of 1h of visible light irradiation, STC4 was found to remove around 0.41 µmol of NO_x, whereas S-TiO_2, NP400, and g-CN removed around 0.13 µmol, 0.31 µmol, and 0.25 µmol, respectively. For NO_3^- selectivity under visible light, a similar pattern was observed as photooxidation under UV light. Initially, selectivity increased with the increase in the precursor mix's melamine content, and after 80%, it started to decrease.

3.2 Morphological attributes

3.2.1 XRD and BET analysis

XRD was conducted to identify the phase configuration of the synthesized samples as tabulated in Table 1, and the patterns were compared with commercially available NP400 and laboratory prepared g-CN and S-TiO_2. Fig. 2(b) shows that the prepared S-TiO_2 using dye wastewater is mainly of anatase form. The corresponding anatase crystal planes that were found are, (101), (103), (004), (112), (200), (105), (211), (204), (116), (220), (215), and (224) (JCPDS No. 21-1272) (Xia et al., 2019; Zhang et al., 2019b; Yu et al., 2020). On the other hand, the g-CN prepared in this study showed two characteristic peaks around 2θ of 13.04° and 27.58°, representing the spacing between the adjacent lattice planes of 0.693 and 0.324 nm respectively (Wang et al., 2015). The dominant crystal plans observed in g-CN are depicted in Fig. 2(b), where plane (100) corresponds to the N-bridged repetition of $C_6H_3N_7$ units and (600) explains the inter-planer assembling of the conjugated aromatic system (Dong et al., 2015).

From Fig. 2(a), it is obvious that the synthesized S-TiO_2/g-CN heterojunction preserved the anatase planes of S-TiO_2, and no significant shift in 2θ was observed. Additionally, the peaks for anatase planes remained intact irrespective of the variations in weight ratios of S-TiO_2 and melamine in the precursor mix, which are in coherence with relevant studies (Tan et al., 2018; Troppová et al., 2018; Wang et al., 2018b). At lower melamine content of almost up to 50% of the precursor mix, no characteristic XRD pattern of g-CN was found within the prepared samples. Presumably, this could be due to the formation of negligible amounts of g-CN in the samples. However, once the melamine proportion was twice than that of S-TiO_2 in the precursor mix, an obvious peak around 27.58° (2θ) depicted the presence of

characteristics (002) plane of g-CN. With a further increase in melamine content during the synthesis of the samples, the peak around 27.58° became wider and steeper. The enhancement in peak intensity for g-CN in the consecutive samples (STC1 to STC6) could be attributed to the better crystallinity (Dong et al., 2015).

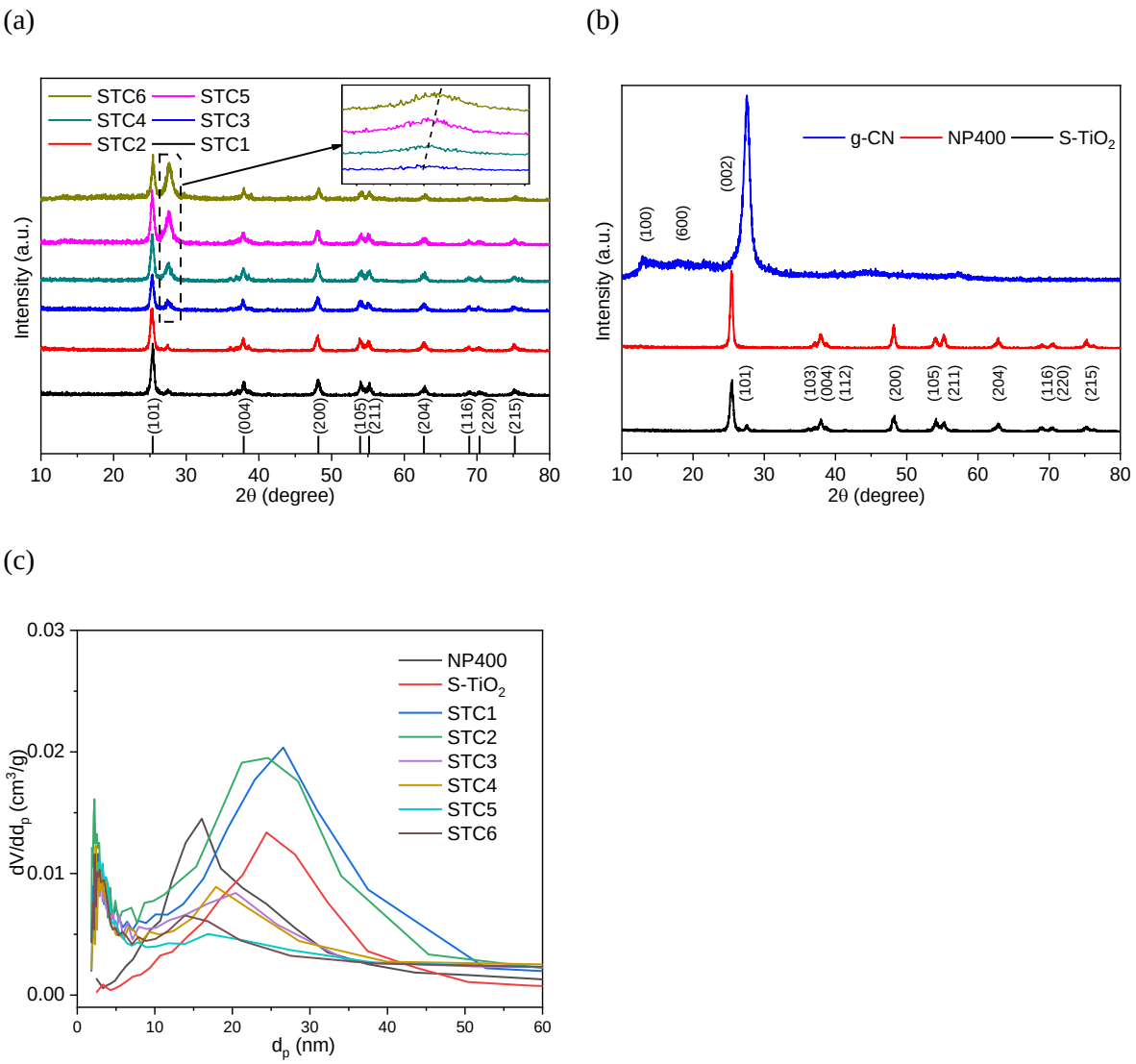

Fig. 2. XRD images of the (a) as-prepared samples STC1 to STC6, and (b) NP400, g-CN and S-TiO_2; (c) evaluated pore size distribution (BJH adsorption) of the as-prepared samples.

Additionally, with the increased content of g-CN in the samples, the (002) lattice plane of g-CN tends to shift slightly toward high 2θ value, due to the reduced gallery distance of the basic aromatic sheets in g-CN. Moreover, due to slight increase in the total content (see Table 1) of the precursor mix, there could be a slight increase in the internal temperature during the synthesis, which could be the

reason behind the slight shift of the (002) plane of the composited g-CN (Dong et al., 2015; Wang et al., 2015). More melamine in the precursor mix will also generate more ammonia, HCN and CN_x gases which renders the atmosphere in furnace were more reductive. Compared to standalone calcination of melamine, the calcination of S-TiO_2 mixed melamine tends to destroy the in-plane periodic $C_6H_3N_7$ units; hence, the lattice plane of g-CN around 13.04° was diminished in the as-prepared samples (Kočí et al., 2017). From the above discussion and by using Fig. 2, it is evident that the prepared samples exhibited superposition of the characteristics XRD peaks of both S-TiO_2 and g-CN. Hence, it can be presumed that during the calcination of the dry mix of S-TiO_2 and melamine, g-CN was assembled on the facade of S-TiO_2, without affecting the crystal lattice arrangement of either of the components.

Moreover, to evaluate the effects on crystal size of the as-synthesized samples, scherrer's equation (Song et al., 2016; Giannakopoulou et al., 2017; Papailias et al., 2017) was utilized at the dominant plane (101) of the anatase TiO_2, and the results are reported in Table 2.

$$D = \frac{K\lambda}{FWHM \times cos\theta} \quad (8)$$

Here, D represents the crystal size, while K, λ, FWHM, and θ are the Scherrer's constant, wavelength, full width at half maxima, and Bragg's angle. From the crystal sizes reported in Table 2, incorporation of g-CN with S-TiO_2 did not show any remarkable changes. The average crystal size of the synthesized samples was determined as 15.42 ± 0.66 nm, which was similar to the pristine S-TiO_2 (15.40 nm).

The effective surface area (S_{BET}) and pore size (d_p) distribution of the as-prepared samples and pristine S-TiO_2 were determined by utilizing N_2 physisorption isotherms. Table 2 depicted the respective S_{BET} values and pore volumes (V_T) of the as-synthesized samples. Furthermore, the d_p distribution curves evaluated using BJH technique were incorporated in Fig. 2(c). S-TiO_2 showed a comparable surface area to commercially available NP400. From the S_{BET} values tabulated in Table 2, a declining trend was observed with the increase of g-CN content in the synthesized samples. Besides, from Fig. 2(c) it is evident that both S-TiO_2 and NP400 showed mesoporous traits, where integration of g-CN in the samples showed the combination of mesoporous and microporous nature (pore size distribution of STC1 – STC4).

Table 2. Estimated FWHM and crystal size of the samples along the dominant anatase (101) plan of TiO_2, effective surface area (S_{BET}), and total pore volume (V_T).

ID	2θ (degree)	FWHM	Crystal size (nm)	S_{BET} (m^2/g)	V_T (cm^3/g)
S-TiO_2	25.41	0.529	15.40	51.69	0.31
STC1	25.31	0.475	16.23	45.45	0.31
STC2	25.28	0.548	14.87	52.33	0.31
STC3	25.31	0.533	15.29	35.0	0.29
STC4	25.33	0.501	16.26	33.69	0.26
STC5	25.34	0.550	14.80	30.47	0.23
STC6	25.44	0.540	15.08	30.40	0.23
NP400	25.40	0.370	21.87	66.65	0.34

3.2.2 FT-IR spectra

To further validate the occurrence of S-TiO_2 and g-CN in the as-synthesized samples, Fourier-transform infrared spectroscopy (FT-IR) analysis was conducted, and the findings were compared with individual FT-IR of S-TiO_2, NP400, and g-CN. The FT-IR spectra of the synthesized samples STC1 – STC6 are illustrated in Fig. 3(a), while Fig. 3(b) depicted the FT-IR patterns of S-TiO_2, NP400, and g-CN. For S-TiO_2 and NP400, the broad absorption peak across 400 – 700 cm^{-1} (Fig. 3(b)) can be allocated to the Ti-O and Ti-O-Ti stretching forms (Liu et al., 2019). Additionally, the broad absorption band around 3000 – 3700 cm^{-1} can be ascribed to the O-H stretching of the adsorbed H_2O on the samples (Kočí et al., 2017; Papailias et al., 2017). The prepared g-CN showed FT-IR peaks around 808.24 cm^{-1} due to the bending mode of skeletal triazine cycles (Zhang et al., 2018a). For g-CN, a series of absorption bands were found within the wavelength range of 1200 – 1600 cm^{-1}, as shown in Fig. 3(b), which are mainly attributed to the C-N stretching of the aromatic part (Troppová et al., 2018). Besides, the wide absorption band within 3000 – 3500 cm^{-1} could also be due to the vibration of N-H from the remaining NH_2 groups (Du et al., 2019).

From Fig. 3(a), STC1 and STC2 only showed the characteristics absorption bands for Ti-O and Ti-O-Ti stretching modes, whereas presence of g-CN was not confirmed which corresponds well with the obtained XRD data. On the other hand, all other samples starting from STC3 to STC6 evidently showed the absorption bands for the aromatic C-N stretching and anatase TiO_2. Additionally, with increased g-CN content in the synthesized samples, the comparative intensity of the characteristics FT-IR peaks for g-CN became broader and steeper. Another interesting finding from assessing the FT-IR spectra of the prepared samples was a slight shift of the wide peak across 400 – 700 cm^{-1} towards greater wavenumber (see Fig. 3(a)), which is in coherence with relevant composite studies (Song et al., 2016; Giannakopoulou et al., 2017). Presumably, the presence of g-CN in the sample modified the chemical environment on the surface of S-TiO_2, and relevant studies confirmed that interaction between the molecular orbitals of the separate components happens due to close heterojunction (Song et al., 2016). Hence, the shift in the Ti-O-Ti stretching modes of the as-synthesized samples may infer robust heterojunction at the edge of S-TiO_2 and g-CN.

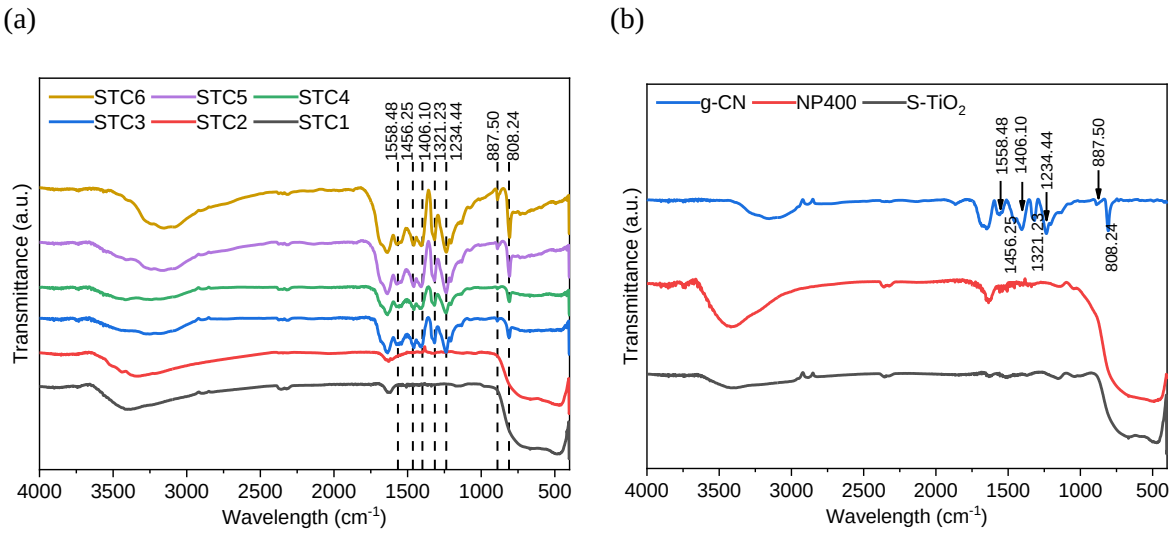

Fig. 3. FT-IR patterns of the (a) as-prepared samples STC1 to STC6, and (b) NP400, g-CN and S-TiO_2.

3.2.3 Electron Microscopy

To authenticate the compositions and morphology of the as-prepared samples, scanning electron microscope (SEM) was conducted, and the SEM images of STC1 to STC6 are illustrated in Fig. S4(a – f). Additionally, for comparison purposes, SEM images of S-TiO_2 and g-CN are incorporated in Fig.

S4(g) and (h), respectively. As a representative of the as-prepared samples transmission electron microscopy (TEM) image of STC4 is incorporated in Fig. 4 at varying magnifications. The prepared g-CN exhibited the presence of a 2D layer sheet structure together with a fairly smooth and flat facade, where the S-TiO_2 prepared from wastewater was found as irregular structure (Fig. 4(a)). From Fig. S5, based on the energy-dispersive X-ray spectroscopy (EDX) results, S-TiO_2 showed the presence of the C atom (8.50%), which is in coherence with former relevant research (Shon et al., 2007). In a number of previous studies, recovered TiO_2 from wastewater sludge inferred the presence of doped C in the as-prepared samples, and the presence of prevailing organic compounds was concluded as the source of the doped C atoms (Shon et al., 2007; Shon et al., 2009a).

By observing the SEM image of STC1 to STC6 (Fig. S4), it is clear that the incorporation of melamine in the precursor mix reduced the agglomeration of S-TiO_2 NPs and more uniform dispersion was observed (Giannakopoulou et al., 2017). Accordingly, based on the EDX result presented in Fig. S5, the presence of C, N, O, and Ti atoms was confirmed in the samples, and with increased melamine content during synthesis, the proportion of g-CN tends to increase. Based on the EDX and SEM results, no g-CN were formed in the STC1 and STC2; however, the presence of C atoms was observed in the as-prepared samples. Initially, by comparing S-TiO_2 and STC1, the atomic proportion of C was reduced from 8.50% to 5%. Further increase of melamine in STC2, enhanced the C content (7.37%) of the sample.

In STC3, i.e., in the initial mix while the melamine content was 150% of S-TiO_2, the occurrence of g-CN was observed in the TEM and EDX (Fig. S5) results. As shown in Fig. 4, the TEM of STC4, depicted the presence of 2D sheet like g-CN along with a considerable amount of somewhat spaced sphere-shaped NPs (S-TiO_2). Moreover, in the TEM image of STC4, transparent lattice fringes at a distance of 0.352 and 0.238 nm were detected, which can be assigned to the anatase lattice planes (101) and (004), respectively (Zhang et al., 2014; Wei et al., 2016).

The TEM image of STC4 (Fig. 4) and SEM image of STC3-STC6 (Fig. S4) explicitly showed the successful grafting of S-TiO_2 over the g-CN nanosheets. In the as-prepared samples, S-TiO_2 NPs appear denser and more compact due to the excellent heterojunction effect and found beneficial for the transfer

of photogenerated e^-/h^+ pairs. The TEM image shows laminar structure of g-CN, loaded with dense and uniformly distributed S-TiO_2 NPs without any apparent accumulation, demonstrating a strong fusion between S-TiO_2 and g-CN.

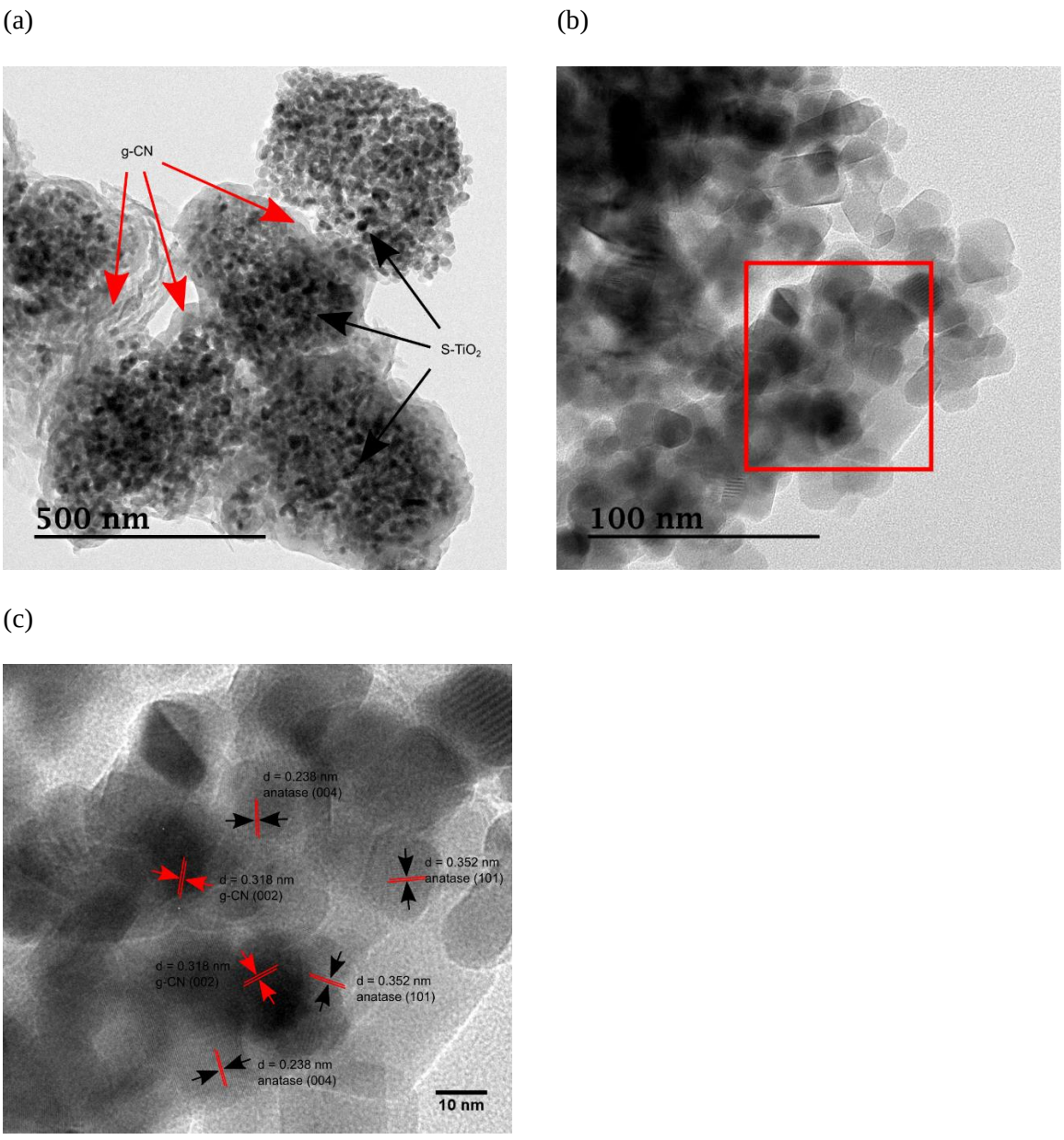

Fig. 4. TEM images of the as-prepared STC4 at varying scale ((a) 500 nm, (b) 100 nm, and (c) 10 nm) showing the presence of S-TiO_2 and g-CN.

3.2.4 XPS spectra

To have an in-depth idea concerning the oxidation states and the chemical compositions of the prevailing components in the as-synthesized samples, X-ray photoelectron spectroscopy (XPS) analysis

was conducted. Fig. S6 illuminated the wide-angle XPS survey spectra of the as synthesized samples. From the Fig. S6, the sharp photoelectron peaks for C 1s, N 1s, Ti 2p, and O 1s are clearly visible across the binding strengths of 286, 400, 458, and 530 eV (Li et al., 2015; Liu et al., 2019). Based on the survey spectra, peaks for Ti 2p and O 1s has significantly reduced in the samples STC5 and STC6. Besides, the prepared g-CN revealed the characteristics C 1s and N 1s peaks on the wide-angle survey scan.

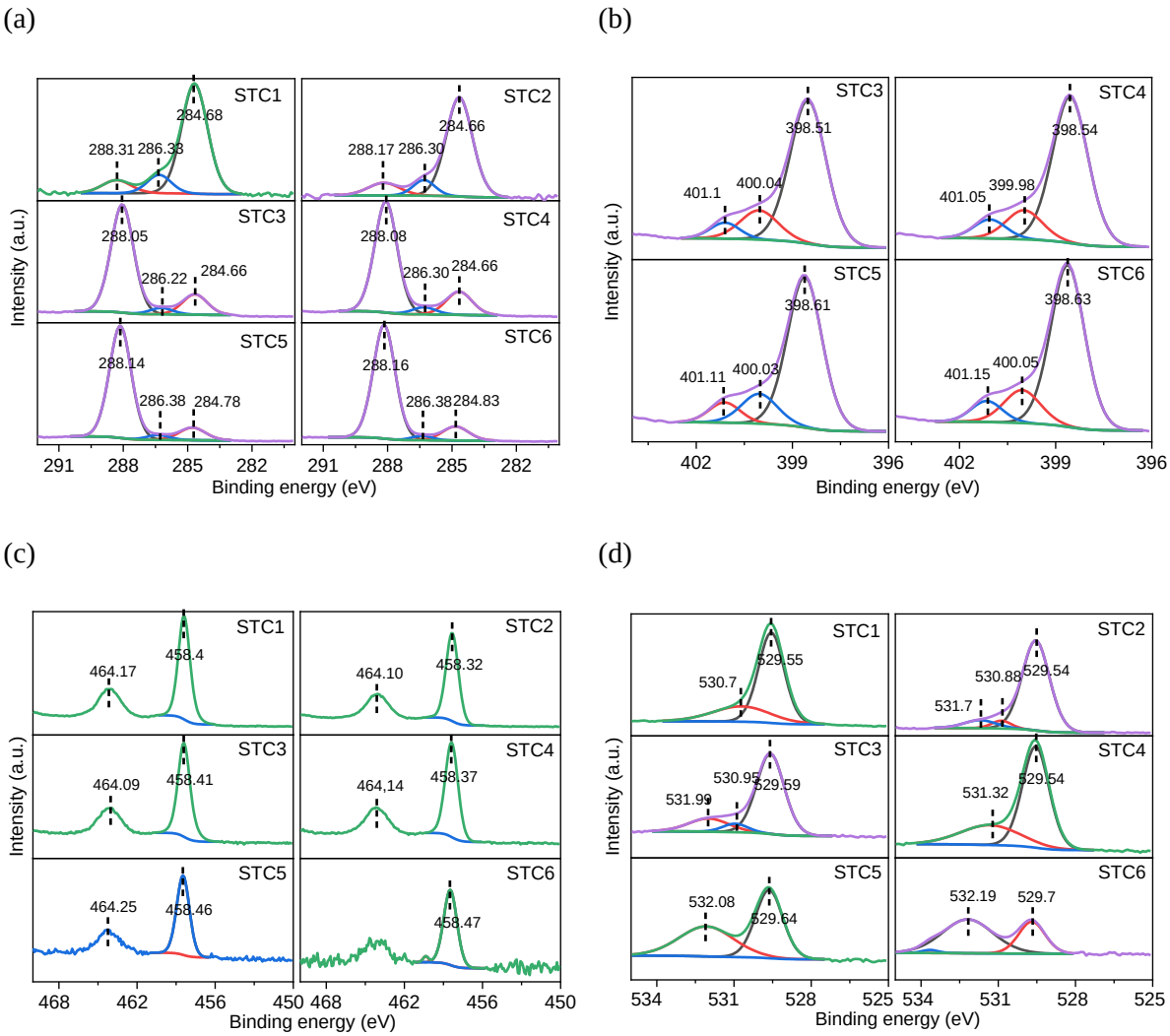

Fig. 5. High resolution survey scan of (a) C 1s, (b) N 1s, (c) Ti 2p, and (d) O 1s for the synthesized STC1 to STC6.

Fig. 5(a – d) shows the high-resolution survey spectra C 1s, N 1s, Ti 2p, and O 1s, respectively, for the as-prepared samples STC1 to STC6. Besides, the peak positions, along with the atomic proportions of the narrow scans for the corresponding samples, are tabulated in Table S3. Lorentz peak fitting was utilized for the deconvolution of the narrow scan XPS peaks. Based on the FT-IR and XRD

analysis, the presence of g-CN was not found in STC1 and STC2; hence the deconvoluted 3 C 1s peaks shown in Fig 5(a) could be attributed to adventitious carbon as Sp^2 hybridized C-C (284.70 eV), C-O-C (286.30 eV) and O-C=O (288.20 eV) bond present as defects (Zhou et al., 2014). While for the prepared g-CN, STC3, STC4, STC5, and STC6, the dominant C 1s narrow scan peak was found around ~288.10 eV, which can be assigned to N-C=N_2 coordination and characteristics peak for g-CN (Thomas et al., 2008; Liu et al., 2019). Additionally, the absence of no visible peak for C-Ti confirmed that there were no chemical reactions between S-TiO_2 and g-CN, rather successful heterojunction was prepared.

Except for STC1 and STC2, from the narrow survey N 1s spectra of the as-synthesized samples dominant peak for triazine rings, i.e., sp^2 hybridized C=N-C was found around ~398.54 eV (Caudillo-Flores et al., 2019). Moreover, peaks for tertiary N-$(C)_3$ and N-H group were found around ~399.98 and 401.05 eV(Li et al., 2019; Liu et al., 2019). Moreover, the peak positions were in coherence with the laboratory-made g-CN (Table S3). In STC1 and STC2, characteristic peaks for g-CN were absent, and very low concentration of N atoms was found in doped condition, which was 0.8% and 0.7%, respectively, which could be the reason for enhanced NO_x removal beneath UV light. The O 1s spectra of the as-prepared samples could mainly be fitted around 529.55 and 530.7 eV, which clearly confirms the presence of lattice O^{2-} and O_2^- ions/OH^- groups respectively (Huang et al., 2019).With the increase of g-CN in the prepared samples, the peak around 530.7 eV tends to shift towards higher binding energy, which inferred that g-CN firmly combines with the oxygen groups presented on the facade of S-TiO_2. Fig. 5(b) indicates the Ti 2p bands of the as-prepared samples STC1 to STC6. Sharp peaks around 458.66 and 464.41 eV has been observed in the samples, which are characteristic peaks of Ti 2p3/2 and Ti 2p1/2 and confirms that Ti is present as Ti^{4+} species (Song et al., 2016). Compared to S-TiO_2, with increased amounts of g-CN in the samples, a negative shift was observed in the prepared samples (Table S3). This phenomenon can be attributed to the close electronic interaction between the used S-TiO_2 and g-CN, which confirms compact sample formation. Additionally, the negative shift could be due to the increased electron density on Ti from the sample formation.

3.2.5 Optical traits and photocatalytic mechanism

Based on the detailed morphological and chemical characterizations, STC3, STC4, STC5, and STC6 were the successful S-TiO_2/g-CN heterojunctions. Additionally, among the aforementioned samples, maximum photoactivity was observed by STC4 under both UV and visible light irradiance (see Fig. 1). Therefore, to further evaluate the photooxidation mechanism of STC4, PL analysis was performed, and the respective spectrum was compared with PL spectra of S-TiO_2 and g-CN (Fig. 6(a)). It is well established that the PL spectra of the semiconductors can infer valuable insights on the rate of photoinduced charge separation, while irradiated with light.

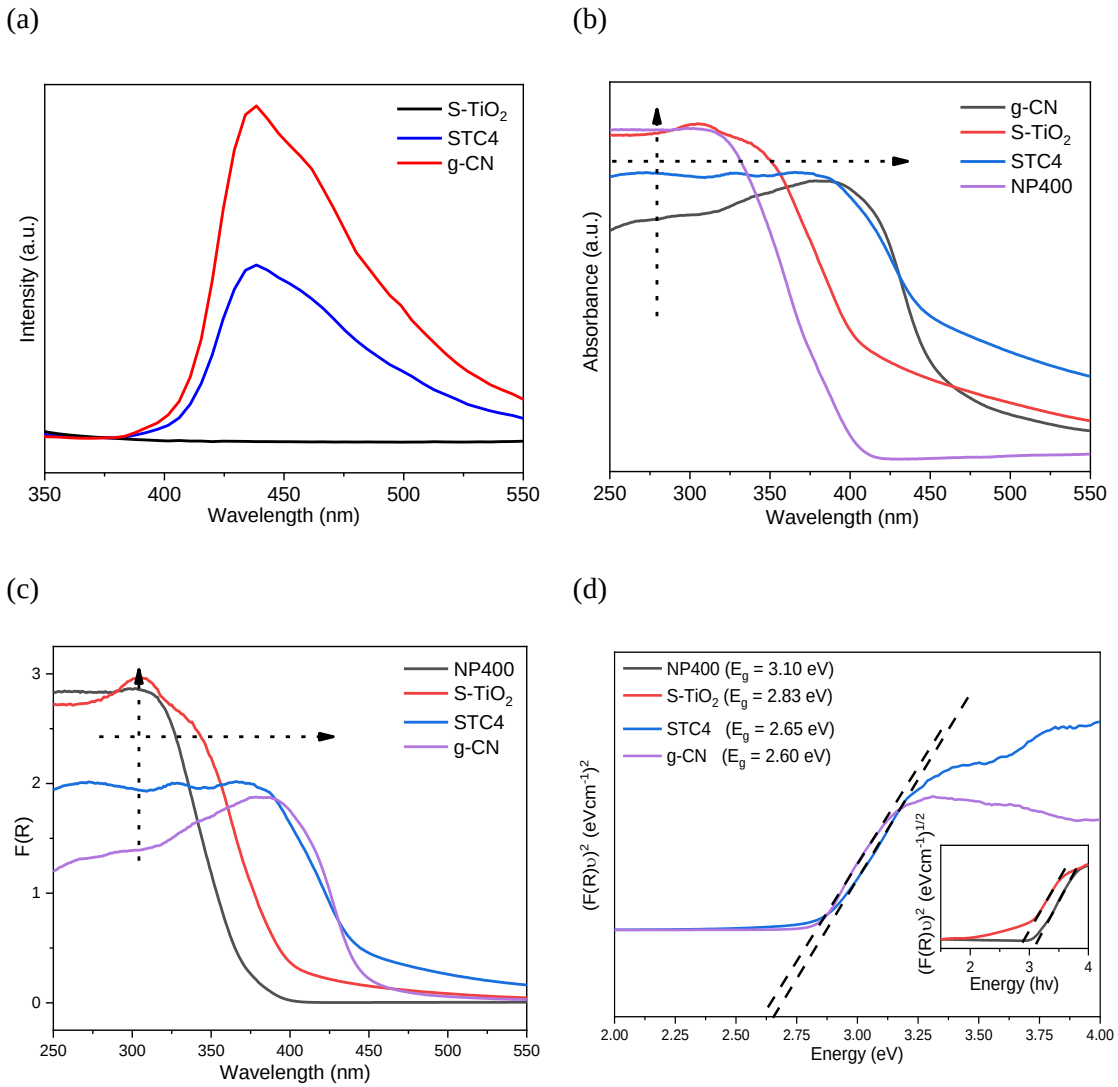

Fig. 6. (a) PL spectra, (b) UV-vis DRS (absorbance vs. wavelength), (c) UV-vis DRS (F(R) vs. wavelength), (d) converted Kubelka-Munk function vs. energy of absorbed light of STC4, S-TiO_2, g-CN, and NP400.

The prepared g-CN displayed a strong quasi-asymmetric PL spectrum, and the maximum peak was found around ~400 nm. This peak corresponds to the recombination of photoinduced e^-/h^+ pairs generated within the g-CN (Wang et al., 2013; Yu et al., 2013). Based on Fig. 6(a), compared to g-CN, STC4 showed much lower PL intensity at a similar peak position. Normally, lower PL intensity means a lower rate of recombination (Troppová et al., 2018). Moreover, the minimal recombination rate of S-TiO_2 is understandable as in the visible light spectrum, light absorption by S-TiO_2 was also minimal.

Additionally, for the determination of the optical energy bandgap (E_g) of STC4, UV-vis DRS was employed, and the light absorption data was reported in the UV-Vis range. By using the extrapolation technique on the modified Kubelka-Munk function, E_g for STC4 was determined, and the findings are depicted in Fig 6(b – d) (Giannakopoulou et al., 2017). Fig. 6(b) and (c) illustrate the absorbance spectra and the pattern of F(R) function of the as-prepared superior sample (STC4), and the results were compared with g-CN, S-TiO_2, and commercially available NP400. From Fig. 6(b), the prepared STC4 showed superior light absorption in the UV region compared to g-CN hence showed significant improvement in removing NO_x under UV light irradiation. On the other hand, compared to NP400 and S-TiO_2, STC4 showed expanded light absorption beyond the UV range. A superposition of the material's light absorption spectra was observed, which also confirmed successful heterojunction. Similar attributes were reported for the photocatalysts synthesized by heterojunction of commercially available titania and nitrogen enriched precursors like (melamine, urea etc.) (Song et al., 2016; Papailias et al., 2017). Additionally, Fig. 6(d) shows the $(F(R)h\nu)^n$ (n = 1/2 and 2) vs. hν graph of the samples, and the energy bandgaps were determined through the extrapolation of the corresponding graphs. The energy bandgaps were determined as 2.60, 2.65, 2.83, and 3.10 eV for g-CN, STC4, S-TiO_2, and NP400, respectively. Besides, the CB and VB edge of S-TiO_2 and g-CN was estimated by using the following equations (Zhou et al., 2019),

$$E_{CB} = E_{VB} - E_g \quad (9)$$

$$E_{VB} = X - E_0 + 0.5\,E_g \quad (10)$$

Here, E_{CB} and E_{VB} represents the CB and VB edge of the semiconductor. Additionally, X and E_0 represents the average electronegativity and the energy of a free electrons next to NHE.

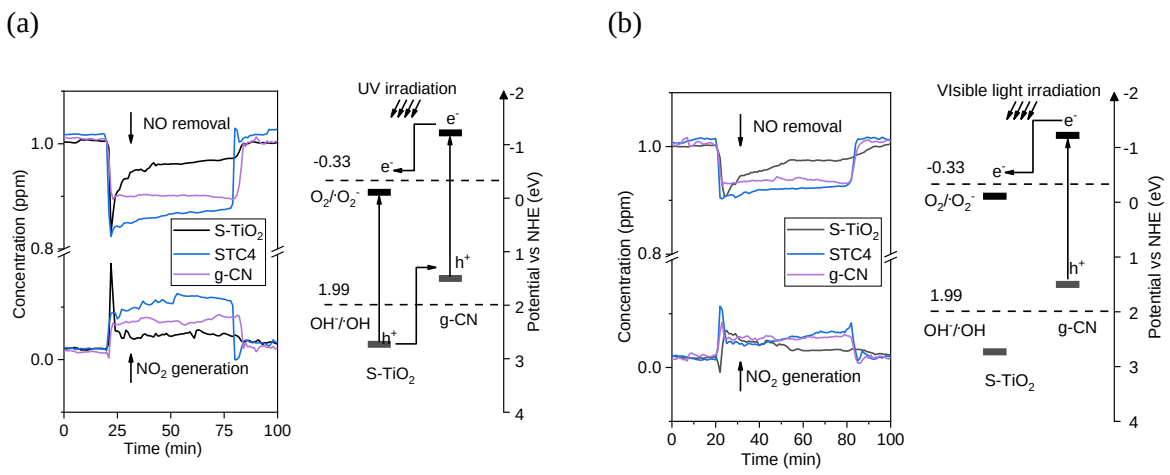

Fig. 7. Proposed photooxidation scheme for NO_x using S-TiO_2/g-CN under UV (a) and visible light (b) irradiation.

Based on the relevant studies, for anatase TiO_2 and g-CN, the value of electronegativity can be assigned as 5.81, and 4.64 eV, respectively, and E_0 can be taken as 4.5 eV (Zhou et al., 2019). Hence, the E_{VB} of S-TiO_2 and g-CN can be estimated as +2.73 eV and +1.5 eV, respectively; also, the corresponding E_{CB} will be -0.11 eV and -1.22 eV. According to the above discussion, the primary factor that has been contributed towards the superior photoactivity of STC4 was the reduced energy bandgap due to the successful formation of heterojunction. Interestingly, despite having reduced S_{BET}, STC4 (33.69 m^2/g) showed extended NO_x oxidation compared to S-TiO_2 (51.69 m^2/g). The possible reason for negligible photoactivity of the prepared S-TiO_2 could be the result of a greater amount of adventitious carbon or Sp2 hybridized defects, as explained with EDX and XPS analysis. On the other hand, the reduced PL intensity of STC4 compared to g-CN confirms the reduced recombination rate; hence, enhanced photoactivity. Based on the assessment of the optical traits of the prepared STC4, the photocatalytic reaction mechanism can be proposed as shown in Fig. 7.

Under UV irradiance, both S-TiO_2 and g-CN within the as-synthesized sample get excited, and the photoinduced e^- transfer from the VB towards the CB of the respective components (Troppová et al., 2018). Hence, the photoinduced e^-/h^+ pair gets generated, as shown in Fig 7(a). Following the charge

separation, the e^- generated on the CB of g-CN favors transferring towards the CB of S-TiO_2 due to less negative CB edge (Song et al., 2016). On the other hand, the h^+ generated on the VB of S-TiO_2 migrates towards the less positive VB of g-CN (Papailias et al., 2017). Consequently, the lifetime of the photoinduced e^-/h^+ pairs gets increased, leading to superior photoactivity. From the inhibited PL spectrum of the as-synthesized STC4, it is evident that the photoinduced charge separation rate got augmented, leading to an enhanced lifetime of e^-/h^+ pairs (Ma et al., 2016). Later, the photoinduced e^- can readily reduce the adjacent O_2 into $\cdot O_2^-$, while the h^+ on the VB reacts with adsorbed H_2O and generates $\cdot OH$ radicals (Ma et al., 2016; Papailias et al., 2017). It is well established that the active species $\cdot O_2^-$ and $\cdot OH$ are the two significant radicals that can promptly oxidize NO_x into more neutral nitrate salts. However, when STC4 was irradiated under visible light, only g-CN became excited, and the photoinduced e^-/h^+ pairs were generated on the respective CB and VB (Ma et al., 2016). Similarly, due to the less negative position of the CB of S-TiO_2, the e^- from g-CN migrates to the S-TiO_2 and restrain the rate of charge recombination. Later, the photoinduced e^-/h^+ pairs can readily produce the active species ($\cdot O_2^-$ and $\cdot OH$) for the effective photooxidation of NO_x. Hence, under UV and visible light irradiation the dominant photocatalytic reactions could be as follows,

$$e^- + O_2 \rightarrow .O_2^- \quad (11)$$

$$h^+ + H_2O\ (OH^-) \rightarrow .OH \quad (12)$$

$$.O_2^- + NO \rightarrow NO_3^- \quad (13)$$

$$.OH + NO \rightarrow NO_2 \quad (14)$$

$$NO_2 + .OH \rightarrow NO_3^- \quad (15)$$

One interesting phenomenon observed during the Photooxidation of NO under UV/visible light was an enhancement in the $NO_3^-{}_{selectivity}$ of the prepared heterojunctions compared to the precursor S-TiO_2. Under UV and visible light irradiation, the $NO_3^-{}_{selectivity}$ of S-TiO_2 was reported as 41.90% (see Table S1) and 42.20% (see Table S2), respectively, which was substantially increased for STC4 and were found as 56.66% and 56.76%, respectively. Perhaps the incorporation of g-CN played a vital role due to the favorable V_{CB}/V_{VB} position. Compared to S-TiO_2 (-0.11 eV), the CB edge of g-CN (-1.22 eV)

was found more negative; hence, the reduction potential of the photogenerated e^- in STC4 was higher to reduce O_2 into $\cdot O_2^-$ (Wang et al., 2016). On the other hand, less positive V_{VB} of g-CN (+1.5 eV) in STC4 reduced the generation rate of $\cdot OH$, as the redox potential of $OH^-/\cdot OH$ (2.37 eV) is higher (Wang et al., 2016; Hossain et al., 2021). Therefore, it can be presumed that the $\cdot O_2^-$ played the primary role in the complete photooxidation of NO. Moreover, the enhanced $NO_3^-{}_{selectivity}$ of STC4 depicted that compared to $\cdot OH$, the oxidation potential of $\cdot O_2^-$ for NO to NO_3^- conversion is higher, explaining the significant NO_2 generation during standalone use of S-TiO_2. The aforementioned phenomena are coherent with most of the TiO_2/g-CN based atmospheric NO removal studies, where $\cdot O_2^-$ was claimed to be the primary reactive species (Ma et al., 2016; Wang et al., 2016; Papailias et al., 2017; Jiang et al., 2018).

4 Conclusion

The objectives of the study were to prepare TiO_2/g-CN samples by utilizing sludge generated TiO_2 and increase the removal of atmospheric NO_x under UV and visible light irradiation. Successful preparation of S-TiO_2/g-CN samples was confirmed through XRD, SEM, TEM, FT-IR, and XPS analysis. Detailed surface characterizations revealed, improved dispersion of S-TiO_2, while sampled with g-CN. Moreover, g-CN had negligible impacts on the crystal structure and size of the utilized S-TiO_2 precursor. Among the successfully prepared samples, maximum NO_x removal was reported for STC4, wherein the precursor mix of the melamine content was 3 times higher than the S-TiO_2. UV-vis DRS conducted on STC4 revealed that the energy bandgap was reduced to 2.65 eV from 3.20 eV from S-TiO_2. Hence, the absorption band of STC4 was significantly increased in both UV and visible regions. Besides, PL analysis showed inhibited recombination rate of generated e^-/h^+ pairs, which is favorable to readily generate $\cdot O_2^-$ and $\cdot OH$ radicals for photodegradation of NO_x. Finally, based on the evaluated optical traits, a simplified schematic is proposed for NO_x removal under UV and visible light irradiation. By considering NO_3^- selectivity, the NO_x removal under UV light by S-TiO_2 was reported only 2.45%, which was increased in STC4 and found as 7.2%. Again, under visible light, the NO_x removal of 1.75% by S-TiO_2 was increased to 5.4% by utilizing STC4. However, compared to commercially available NP400, the NO_x removal of STC4 was found inferior, but this synthesis route of TiO_2/g-CN

heterojunction has significant potential to promote sustainability through the utilization of unwanted sludge from the water treatment plant and reduction in synthesis cost of the photocatalysts.

Author Contributions

Conceptualization and methodology, S.M.H., H.P. and J.S.M.; data analysis, investigation and data curation, S.M.H., J.S.M. and I.R.; original draft writing, S.M.H.; review and editing, L.T., H.-J.K., Y.-S.J. and H.K.S.; supervision, J.-H.K., H.K.S and Y.-S.J. All authors provided critical feedback and helped shape the research, analysis and manuscript.

Acknowledgements

This research was supported by a grant (18SCIP-B145909-01) from Smart Civil Infrastructure Research Program funded by Ministry of Land, Infrastructure and Transport of Korean government and Photo & Environmental Technology Co., Ltd.

References

Asahi, R., Morikawa, T., Irie, H., Ohwaki, T., 2014. Nitrogen-doped titanium dioxide as visible-light-sensitive photocatalyst: designs, developments, and prospects. Chem Rev 114, 9824-9852.

Aziz, H.A., Razak, M.H.A., Rahim, M.Z.A., Kamar, W., Abu Amr, S.S., Hussain, S., Van Leeuwen, J., 2018. Evaluation and comparison the performance of titanium and zirconium(IV) tetrachloride in textile wastewater treatment. Data Brief 18, 920-927.

Caudillo-Flores, U., Muñoz-Batista, M.J., Luque, R., Fernández-García, M., Kubacka, A., 2019. g-C3N4/TiO2 composite catalysts for the photo-oxidation of toluene: Chemical and charge handling effects. Chemical Engineering Journal 378.

Chi, Y., Tian, C., Li, H., Zhao, Y., 2019. Polymerized Titanium Salts for Algae-Laden Surface Water Treatment and the Algae-Rich Sludge Recycle toward Chromium and Phenol Degradation from Aqueous Solution. ACS Sustainable Chemistry & Engineering 7, 12964-12972.

Diebold, U., 2003. The surface science of titanium dioxide. Surface Science Reports 48, 53-229.

570 Dong, F., Li, Y., Wang, Z., Ho, W.-K., 2015. Enhanced visible light photocatalytic activity and
571 oxidation ability of porous graphene-like g-C3N4 nanosheets via thermal exfoliation. Applied Surface
572 Science 358, 393-403.
573 Du, X., Bai, X., Xu, L., Yang, L., Jin, P., 2019. Visible-light activation of persulfate by TiO2/g-C3N4
574 photocatalyst toward efficient degradation of micropollutants. Chemical Engineering Journal.
575 El Saliby, I., Okour, Y., Shon, H.K., Kandasamy, J., Lee, W.E., Kim, J.-H., 2012. TiO_2 nanoparticles
576 and nanofibres from $TiCl_4$ flocculated sludge: Characterisation and photocatalytic activity. Journal of
577 Industrial and Engineering Chemistry 18, 1033-1038.
578 El Saliby, I.J., Okour, Y.H., Shon, H.K., Vigneswaran, S., Kandasamy, J., Kim, J.H., 2009. Detailed
579 investigation on the effect of washing TiO_2 prepared from Ti-salts flocculated wastewater sludge.
580 Journal of Advanced Oxidation Technologies 12, 194-201.
581 El Saliby, I.J., Shon, H.K., Okour, Y.H., Vigneswaran, S., Senthilnanthanan, M., Kandasamy, J.,
582 2010. Production of titanium dioxide nanoparticles and nanostructures from dye wastewater sludge -
583 characterisation and evaluation of photocatalytic activity. Journal of Advanced Oxidation
584 Technologies 13, 15-20.
585 Fujishima, A., Honda, K., 1972. Electrochemical Photolysis of Water at a Semiconductor Electrode.
586 Nature 238, 37-38.
587 Giannakopoulou, T., Papailias, I., Todorova, N., Boukos, N., Liu, Y., Yu, J., Trapalis, C., 2017.
588 Tailoring the energy band gap and edges' potentials of g-C_3N_4/TiO_2 composite photocatalysts for NO_x
589 removal. Chemical Engineering Journal 310, 571-580.
590 Haider, Z., Cho, H.I., Moon, G.H., Kim, H.I., 2019. Minireview: Selective production of hydrogen
591 peroxide as a clean oxidant over structurally tailored carbon nitride photocatalysts. Catalysis Today
592 335, 55-64.
593 Hossain, S.M., Park, H., Kang, H.-J., Mun, J.S., Tijing, L., Rhee, I., Kim, J.-H., Jun, Y.-S., Shon,
594 H.K., 2021. Facile synthesis and characterization of anatase TiO2/g-CN composites for enhanced
595 photoactivity under UV–visible spectrum. Chemosphere 262.
596 Huang, J., Li, D., Li, R., Chen, P., Zhang, Q., Liu, H., Lv, W., Liu, G., Feng, Y., 2020. One-step
597 synthesis of phosphorus/oxygen co-doped g-C3N4/anatase TiO2 Z-scheme photocatalyst for

598 significantly enhanced visible-light photocatalysis degradation of enrofloxacin. J Hazard Mater 386,
599 121634.
600 Huang, Y., Wang, P.G., Wang, Z.Y., Rao, Y.F., Cao, J.J., Pu, S.Y., Ho, W.K., Lee, S.C., 2019.
601 Protonated g-C3N4/Ti( )(3+)self-doped TiO2 nanocomposite films: Room-temperature preparation,
602 hydrophilicity, and application for photocatalytic NOx removal. Appl. Catal. B-Environ. 240, 122-
603 131.
604 Hussain, S., Awad, J., Sarkar, B., Chow, C.W.K., Duan, J., Leeuwen, J.v., 2019. Coagulation of
605 dissolved organic matter in surface water by novel titanium (III) chloride: Mechanistic surface
606 chemical and spectroscopic characterisation. Separation and Purification Technology 213, 213-223.
607 Jeon, K.-J., Ahn, J.-H., 2018. Evaluation of titanium tetrachloride and polytitanium tetrachloride to
608 remove phosphorus from wastewater. Separation and Purification Technology 197, 197-201.
609 Jiang, G.M., Cao, J.W., Chen, M., Zhang, X.M., Dong, F., 2018. Photocatalytic NO oxidation on N-
610 doped TiO2/g-C3N4 heterojunction: Enhanced efficiency, mechanism and reaction pathway. Applied
611 Surface Science 458, 77-85.
612 Kim, J.B., Seol, D.H., Shon, H.K., Kim, G.J., Kim, J.H., 2010. Preparation and characterization of
613 titania nanoparticles from titanium tetrachloride and titanium sulfate flocculation of dye wastewater.
614 Journal of the Japan Petroleum Institute 53, 167-172.
615 Kobayakawa, K., Murakami, Y., Sato, Y., 2005. Visible-light active N-doped TiO2 prepared by
616 heating of titanium hydroxide and urea. Journal of Photochemistry and Photobiology A: Chemistry
617 170, 177-179.
618 Kočí, K., Reli, M., Troppová, I., Šihor, M., Kupková, J., Kustrowski, P., Praus, P., 2017.
619 Photocatalytic decomposition of N2O over TiO2/g-C3N4 photocatalysts heterojunction. Applied
620 Surface Science 396, 1685-1695.
621 Kumar, S., Karthikeyan, S., Lee, A.F., 2018. g-C3N4-Based Nanomaterials for Visible Light-Driven
622 Photocatalysis. Catalysts 8, 47.
623 Lee, B.C., Kim, S., Shon, H.K., Vigneswaran, S., Kim, S.D., Cho, J., Kim, I.S., Choi, K.H., Kim, J.B.,
624 Park, H.J., Kim, J.H., 2008. Aquatic toxicity evaluation of TiO_2 nanoparticle produced from sludge of
625 $TiCl_4$ flocculation of wastewater and seawater. Journal of Nanoparticle Research 11, 2087-2096.

626 Li, C., Lou, Z., Yang, Y., Wang, Y., Lu, Y., Ye, Z., Zhu, L., 2019. Hollowsphere Nanoheterojunction
627 of g-C3N4@TiO2 with High Visible Light Photocatalytic Property. Langmuir 35, 779-786.
628 Li, K., Gao, S., Wang, Q., Xu, H., Wang, Z., Huang, B., Dai, Y., Lu, J., 2015. In-Situ-Reduced
629 Synthesis of Ti(3)(+) Self-Doped TiO(2)/g-C(3)N(4) Heterojunctions with High Photocatalytic
630 Performance under LED Light Irradiation. ACS Appl Mater Interfaces 7, 9023-9030.
631 Liu, H., Yu, D.Q., Sun, T.B., Du, H.Y., Jiang, W.T., Muhammad, Y., Huang, L., 2019. Fabrication of
632 surface alkalinized g-C3N4 and TiO2 composite for the synergistic adsorption-photocatalytic
633 degradation of methylene blue. Applied Surface Science 473, 855-863.
634 Ma, J.Z., Wang, C.X., He, H., 2016. Enhanced photocatalytic oxidation of NO over g-C3N4-TiO2
635 under UV and visible light. Appl. Catal. B-Environ. 184, 28-34.
636 Nasirian, M., Lin, Y.P., Bustillo-Lecompte, C.F., Mehrvar, M., 2017. Enhancement of photocatalytic
637 activity of titanium dioxide using non-metal doping methods under visible light: a review.
638 International Journal of Environmental Science and Technology 15, 2009-2032.
639 Okour, Y., El Saliby, I., Shon, H.K., Vigneswaran, S., Kim, J.H., Cho, J., Kim, I.S., 2009a. Recovery
640 of sludge produced from Ti-salt flocculation as pretreatment to seawater reverse osmosis.
641 Desalination 247, 53-63.
642 Okour, Y., Shon, H.K., El Saliby, I., 2009b. Characterisation of titanium tetrachloride and titanium
643 sulfate flocculation in wastewater treatment. Water Sci Technol 59, 2463-2473.
644 Ong, W.J., 2017. 2D/2D Graphitic Carbon Nitride (g-C3N4) Heterojunction Nanocomposites for
645 Photocatalysis: Why Does Face-to-Face Interface Matter? Front. Mater. 4, 10.
646 Papailias, I., Todorova, N., Giannakopoulou, T., Yu, J.G., Dimotikali, D., Trapalis, C., 2017.
647 Photocatalytic activity of modified g-C3N4/TiO2 nanocomposites for NOx removal. Catalysis Today
648 280, 37-44.
649 Park, S.M., Chekli, L., Kim, J.B., Shahid, M., Shon, H.K., Kim, P.S., Lee, W.S., Lee, W.E., Kim,
650 J.H., 2014. NO_x removal of mortar mixed with titania produced from Ti-salt flocculated sludge.
651 Journal of Industrial and Engineering Chemistry 20, 3851-3856.
652 Rhee, I., Lee, J.S., Kim, J.B., Kim, J.H., 2018. Nitrogen oxides mitigation efficiency of cementitious
653 materials incorporated with TiO 2. Materials 11.

Shon, H., Okour, Y., El Saliby, I., Park, J., Cho, D., Kim, J.-B., Park, H.-J., Kim, J.-H., 2009a. Preparation and Characterisation of Titanium dioxide Produced from Ti-salt Flocculated Sludge in Water Treatment. Journal of the Korean Industrial and Engineering Chemistry.

Shon, H., Phuntsho, S., Okour, Y., Cho, D.-L., KK, S., Li, J., Na, S.-H., Kim, J.-B., Kim, J.-H., 2008. Visible light responsive titanium dioxide (TiO_2). Journal of the Korean Industrial and Engineering Chemistry.

Shon, H.K., Vigneswaran, S., Kandasamy, J., Zareie, M.H., Kim, J.B., Cho, D.L., Kim, J.H., 2009b. Preparation and characterization of titanium dioxide (TiO_2) from sludge produced by $TiCl_4$ flocculation with $FeCl_3$, $Al_2(SO_4)_3$ and $Ca(OH)_2$ coagulant aids in wastewater. Separation Science and Technology 44, 1525-1543.

Shon, H.K., Vigneswaran, S., Kim, I.S., Cho, J., Kim, G.J., Kim, J.B., Kim, J.H., 2007. Preparation of titanium dioxide (TiO_2) from sludge produced by titanium tetrachloride ($TiCl_4$) flocculation of wastewater. Environmental Science & Technology 41, 1372-1377.

Song, X., Hu, Y., Zheng, M.M., Wei, C.H., 2016. Solvent-free in situ synthesis of g-C3N4/{001}TiO2 composite with enhanced UV- and visible-light photocatalytic activity for NO oxidation. Appl. Catal. B-Environ. 182, 587-597.

Sun, Y., Zhou, G., Xiong, X., Guan, X., Li, L., Bao, H., 2013. Enhanced arsenite removal from water by $Ti(SO_4)_2$ coagulation. Water Research 47, 4340-4348.

Tan, S., Xing, Z., Zhang, J., Li, Z., Wu, X., Cui, J., Kuang, J., Zhu, Q., Zhou, W., 2018. Ti3+-TiO2/g-C3N4 mesostructured nanosheets heterojunctions as efficient visible-light-driven photocatalysts. Journal of Catalysis 357, 90-99.

Thomas, A., Fischer, A., Goettmann, F., Antonietti, M., Müller, J.-O., Schlögl, R., Carlsson, J.M., 2008. Graphitic carbon nitride materials: variation of structure and morphology and their use as metal-free catalysts. Journal of Materials Chemistry 18.

Troppová, I., Šihor, M., Reli, M., Ritz, M., Praus, P., Kočí, K., 2018. Unconventionally prepared TiO 2 /g-C 3 N 4 photocatalysts for photocatalytic decomposition of nitrous oxide. Applied Surface Science 430, 335-347.

Wan, Y., Huang, X., Shi, B., Shi, J., Hao, H., 2019. Reduction of organic matter and disinfection byproducts formation potential by titanium, aluminum and ferric salts coagulation for micro-polluted source water treatment. Chemosphere 219, 28-35.

Wang, D.J., Saleh, N.B., Sun, W.J., Park, C.M., Shen, C.Y., Aich, N., Peijnenhurg, W., Zhang, W., Jin, Y., Su, C.M., 2019. Next-Generation Multifunctional Carbon-Metal Nanohybrids for Energy and Environmental Applications. Environmental Science & Technology 53, 7265-7287.

Wang, H., Li, J., Ma, C., Guan, Q., Lu, Z., Huo, P., Yan, Y., 2015. Melamine modified P25 with heating method and enhanced the photocatalytic activity on degradation of ciprofloxacin. Applied Surface Science 329, 17-22.

Wang, X.-j., Yang, W.-y., Li, F.-t., Xue, Y.-b., Liu, R.-h., Hao, Y.-j., 2013. In Situ Microwave-Assisted Synthesis of Porous N-TiO2/g-C3N4 Heterojunctions with Enhanced Visible-Light Photocatalytic Properties. Industrial & Engineering Chemistry Research 52, 17140-17150.

Wang, X., Gan, Y., Guo, S., Ma, X., Xu, M., Zhang, S., 2018a. Advantages of titanium xerogel over titanium tetrachloride and polytitanium tetrachloride in coagulation: A mechanism analysis. Water Res 132, 350-360.

Wang, Z., Chen, M., Huang, Y., Shi, X., Zhang, Y., Huang, T., Cao, J., Ho, W., Lee, S.C., 2018b. Self-assembly synthesis of boron-doped graphitic carbon nitride hollow tubes for enhanced photocatalytic NOx removal under visible light. Appl. Catal. B-Environ. 239, 352-361.

Wang, Z., Huang, Y., Ho, W., Cao, J., Shen, Z., Lee, S.C., 2016. Fabrication of Bi2O2CO3/g-C3N4 heterojunctions for efficiently photocatalytic NO in air removal: In-situ self-sacrificial synthesis, characterizations and mechanistic study. Applied Catalysis B: Environmental 199, 123-133.

Wang, Z., Wang, Y., Yu, C., Zhao, Y., Fan, M., Gao, B., 2018c. The removal of silver nanoparticle by titanium tetrachloride and modified sodium alginate composite coagulants: floc properties, membrane fouling, and floc recycle. Environ Sci Pollut Res Int.

Wei, X., Shao, C., Li, X., Lu, N., Wang, K., Zhang, Z., Liu, Y., 2016. Facile in situ synthesis of plasmonic nanoparticles-decorated g-C3N4/TiO2 heterojunction nanofibers and comparison study of their photosynergistic effects for efficient photocatalytic H2 evolution. Nanoscale 8, 11034-11043.

Xia, X., Lan, S., Li, X., Xie, Y., Liang, Y., Yan, P., Chen, Z., Xing, Y., 2018. Characterization and coagulation-flocculation performance of a composite flocculant in high-turbidity drinking water treatment. Chemosphere 206, 701-708.

Xia, Y., Xu, L., Peng, J., Han, J., Guo, S., Zhang, L., Han, Z., Komarneni, S., 2019. TiO2@g-C3N4 core/shell spheres with uniform mesoporous structures for high performance visible-light photocatalytic application. Ceramics International 45, 18844-18851.

Xiao, M., Luo, B., Wang, S.C., Wang, L.Z., 2018. Solar energy conversion on g-C3N4 photocatalyst: Light harvesting, charge separation, and surface kinetics. J. Energy Chem. 27, 1111-1123.

Xu, B.T., Ahmed, M.B., Zhou, J.L., Altaee, A., Xu, G., Wu, M.H., 2018a. Graphitic carbon nitride based nanocomposites for the photocatalysis of organic contaminants under visible irradiation: Progress, limitations and future directions. Science of the Total Environment 633, 546-559.

Xu, J., Zhao, Y., Gao, B., Zhao, Q., 2018b. Enhanced algae removal by Ti-based coagulant: comparison with conventional Al- and Fe-based coagulants. Environmental Science and Pollution Research 25, 13147-13158.

Yu, B., Meng, F., Khan, M.W., Qin, R., Liu, X., 2020. Facile synthesis of AgNPs modified TiO2@g-C3N4 heterojunction composites with enhanced photocatalytic activity under simulated sunlight. Materials Research Bulletin 121.

Yu, J., Wang, S., Low, J., Xiao, W., 2013. Enhanced photocatalytic performance of direct Z-scheme g-C3N4-TiO2 photocatalysts for the decomposition of formaldehyde in air. Phys Chem Chem Phys 15, 16883-16890.

Zhang, B., Wang, Q., Zhuang, J., Guan, S., Li, B., 2018a. Molten salt assisted in-situ synthesis of TiO2/g-C3N4 composites with enhanced visible-light-driven photocatalytic activity and adsorption ability. Journal of Photochemistry and Photobiology A: Chemistry 362, 1-13.

Zhang, L., Jing, D., She, X., Liu, H., Yang, D., Lu, Y., Li, J., Zheng, Z., Guo, L., 2014. Heterojunctions in g-C3N4/TiO2(B) nanofibres with exposed (001) plane and enhanced visible-light photoactivity. J. Mater. Chem. A 2, 2071-2078.

Zhang, S., Gu, P.C., Ma, R., Luo, C.T., Wen, T., Zhao, G.X., Cheng, W.C., Wang, X.K., 2019a. Recent developments in fabrication and structure regulation of visible-light-driven g-C3N4-based photocatalysts towards water purification: A critical review. Catalysis Today 335, 65-77.

Zhang, W., Song, R., Cao, B., Yang, X., Wang, D., Fu, X., Song, Y., 2018b. Variations of floc morphology and extracellular organic matters (EOM) in relation to floc filterability under algae flocculation harvesting using polymeric titanium coagulants (PTCs). Bioresour Technol 256, 350-357.

Zhang, X.B., Song, H.Y., Sun, C.Y., Chen, C.X., Han, F.Q., Li, X.F., 2019b. Photocatalytic oxidative desulfurization and denitrogenation of fuels over sodium doped graphitic carbon nitride nanosheets under visible light irradiation. Materials Chemistry and Physics 226, 34-43.

Zhao, Y.-x., Li, X.-y., 2019. Polymerized titanium salts for municipal wastewater preliminary treatment followed by further purification via crossflow filtration for water reuse. Separation and Purification Technology 211, 207-217.

Zhou, B., Hong, H., Zhang, H., Yu, S., Tian, H., 2019. Heterostructured Ag/g- C3N4/TiO2 with enhanced visible light photocatalytic performances. Journal of Chemical Technology & Biotechnology 94, 3806-3814.

Zhou, S., Liu, Y., Li, J., Wang, Y., Jiang, G., Zhao, Z., Wang, D., Duan, A., Liu, J., Wei, Y., 2014. Facile in situ synthesis of graphitic carbon nitride (g-C3N4)-N-TiO2 heterojunction as an efficient photocatalyst for the selective photoreduction of CO2 to CO. Applied Catalysis B: Environmental 158-159, 20-29.